

# Electrochemical Surface Nanostructuring of $\text{Ti}_{4.7}\text{Cu}_{3.8}\text{Fe}_{2.5}\text{Zr}_{7.5}\text{Sn}_2\text{Si}_1\text{Ag}_2$ Metallic Glass for Improved Pitting Corrosion Resistance

Nora Fernández-Navas,\* Christine Joy Querebillo, Kirti Tiwari, Martin Hantusch, Viktoriia Shtefan, Nicolás Pérez, Paola Rizzi, Martina Zimmermann, and Annett Gebert

Ti-based bulk metallic glasses are envisioned for human implant applications. Yet, while their elevated Cu content is essential for a high glass-forming ability, it poses biocompatibility issues, necessitating a reduction in near-surface regions. To address this, surface treatments that simultaneously generate protective and bioactive states, based on nanostructured Ti and Zr-oxide layers are proposed. An electrochemical pseudo-dealloying process using the bulk glass-forming  $\text{Ti}_{4.7}\text{Cu}_{3.8}\text{Fe}_{2.5}\text{Zr}_{7.5}\text{Sn}_2\text{Si}_1\text{Ag}_2$  alloy is defined. Melt-spun ribbons are immersed in hot concentrated nitric acid solution, monitoring the anodic polarization behavior. From the current density transient measurements, together with surface studies (field-emission scanning electron microscopy, transmission electron microscopy, and Auger electron spectroscopy), the surface reactions are described. This nanostructuring process is divided into three stages: passivation, Cu dissolution, and slow oxide growth, leading to homogenous nanoporous and ligament structures. By tuning the applied potential, the pore and ligament sizes, and thickness values are adjusted. According to X-ray photoelectron spectroscopy, these nanoporous structures are Ti and Zr-oxides rich in hydrous and nonhydrous states. In a simulated physiological solution, for those treated glassy alloy samples, complete suppression of chloride-induced pitting corrosion in the anodic regime of water stability is achieved. This high corrosion resistance is similar to that of clinically used cp-Ti.

present unique chemical properties, including excellent catalytic activity and high corrosion resistance in various environments. These attributes surpass those of conventional crystalline alloys.<sup>[1–3]</sup> Among the glass-forming systems, Ti-based alloys stand out for envisioned biomedical applications, mainly as an implant material in dentistry, trauma surgery, or orthopedics.<sup>[4–8]</sup> They present very high static compressive strengths of  $\sigma_{\text{max}} = 1680\text{--}2640$  MPa, in combination with Young's modulus of  $E = 80\text{--}100$  GPa.<sup>[5,6]</sup> These properties are advantageous compared to implant materials currently in clinical use, such as cp-Ti ( $\sigma_{\text{max}} = 240\text{--}550$  MPa,  $E = 102\text{--}108$  GPa) and Ti-6Al-4V ( $\sigma_{\text{max}} = 860\text{--}950$  MPa,  $E = 110\text{--}114$  GPa) due to the fact that stress-shielding effects and early implant failure can be reduced.<sup>[7–9]</sup>


A high glass-forming ability (GFA) determines the castability of bulk amorphous specimens. This typically requires multicomponent alloy compositions with biocompatible Ti (and/or Zr, Nb) being mixed with cytotoxic elements (Be, Al,

or Ni) or noble metals (Pd, Pt). However, this addition impairs their application as implant materials in the human body.<sup>[8,10,11]</sup> In the last decades, several Ti-based BMG systems free of the abovementioned toxic elements have been developed.<sup>[6,12,13]</sup> One promising biomaterial is the  $\text{Ti}_{4.7}\text{Cu}_{3.8}\text{Fe}_{2.5}\text{Zr}_{7.5}\text{Sn}_2\text{Si}_1\text{Ag}_2$

## 1. Introduction

Bulk metallic glasses (BMGs) have gained considerable research interest in recent years due to their mechanical performance, exhibiting very high strengths and hardness values. They also

N. Fernández-Navas, C. J. Querebillo, M. Hantusch, V. Shtefan, N. Pérez, A. Gebert  
Leibniz-Institute for Solid State and Materials Research Dresden  
(Leibniz IFW Dresden)  
Institute for Materials Chemistry  
Helmholtzstr. 20, 01069 Dresden, Germany  
E-mail: n.fernandez.navas@ifw-dresden.de

 The ORCID identification number(s) for the author(s) of this article can be found under <https://doi.org/10.1002/adem.202302206>.

© 2024 The Authors. Advanced Engineering Materials published by Wiley-VCH GmbH. This is an open access article under the terms of the Creative Commons Attribution License, which permits use, distribution and reproduction in any medium, provided the original work is properly cited.

DOI: 10.1002/adem.202302206

N. Fernández-Navas, M. Zimmermann  
Faculty of Mechanical Science and Engineering  
TU Dresden  
Helmholtzstr. 10, 01069 Dresden, Germany

K. Tiwari, P. Rizzi  
Dipartimento di Chimica and NIS  
Università degli Studi di Torino  
V. Giuria 7, 10125 Torino, Italy

V. Shtefan  
Educational and Scientific Institute of Chemical Technologies and Engineering  
National Technical University "Kharkiv Polytechnic Institute"  
Kyrpychova Str. 2, 61002 Kharkiv, Ukraine

which possesses a high GFA and has been reported to be cast as bulk glassy rods with a diameter of up to 7 mm. This is in addition to affording Young's modulus of  $E = 100$  GPa and a compressive strength of  $\sigma_{\max} = 2080$  MPa.<sup>[14]</sup> Moreover, a great advantage this alloy offers is its ability to be produced in bulk amorphous state by selective laser melting.<sup>[15]</sup> This additive manufacturing technique extends the degree of freedom for BMG sample size and geometry without altering mechanical or corrosion properties,<sup>[16,17]</sup> which is indispensable for biomedical use.

While various publications have already determined a possible implant application for Ti–Cu-based BMGs<sup>[18,19]</sup> as well as for Zr–Cu-based BMGs,<sup>[7]</sup> more critical studies point out the essential problem of their insufficient biocompatibility.<sup>[4,20,21]</sup> Usually a high amount of Cu ( $\geq 30$  at%) is needed in the Ti-alloy composition for bulk glass formation.<sup>[6,8]</sup> Nevertheless, Cu is in general known as a cytotoxic element. As-cast BMG specimens contain significant amounts of Cu in the near-surface region, which can be released in a physiological environment, introducing a risk of inflammatory reactions or death of bone-forming cells.<sup>[8,21–24]</sup> In contrast, Cu has been shown to induce antibacterial effects.<sup>[25]</sup> Additionally, the high Cu content of Ti- and of similar Zr-based BMGs is a driving force of chloride-induced pitting corrosion, which affects the mechanical integrity of bulk samples.<sup>[5,8,26–28]</sup> Chloride-induced stress corrosion and corrosion fatigue problems have been discussed in initial studies in this field.<sup>[29–32]</sup> These BMG corrosion problems hold disadvantages compared to highly resistant alternative implant materials, e.g., Ti, Ti-6Al-4V, new beta-type Ti-alloys, or simple Ti-based glass-formers with only valve-metal-type components.<sup>[8,14,33,34]</sup> Variations such as partial substitution of critical Cu with more resistant elements, for instance Nb or Ga, can only inhibit but not suppress pitting. Moreover, they deteriorate the GFA.<sup>[26,35]</sup> Altogether, Cu plays a crucial role in obtaining monolithic bulk glasses, ensuring favorable mechanical performance. Nevertheless, to mitigate biocompatibility issues, it is necessary to significantly decrease the Cu content in the near-surface regions of the specimens. This can be accomplished through appropriate physio-chemical surface treatments applied to the established glassy alloy compositions.

Ti and classical Ti-alloys form spontaneous barrier-type passivation layers consisting of Ti oxides with only a few nanometer thicknesses. They provide high corrosion stability but they are bioinert. For permanent implants, the creation of bioactive conditions is crucial in achieving optimal growth of bone tissue. The roughness, topography, surface energy, and chemistry of the metal surface can be used to control the processes at the implant-tissue interface.<sup>[36–39]</sup> Conversely, established surface treatments for Ti-based biomaterials are mostly not applicable to the BMG class. Initial studies have proposed chemical surface processing methods for Ti–Cu-based BMGs.<sup>[4,5,7]</sup> For example, Qin et al. deposited pure titanium films by magneto-sputtering on the  $\text{Ti}_{40}\text{Zr}_{10}\text{Cu}_{36}\text{Pd}_{14}$  BMG surface to enhance apatite formation in simulated body fluid (SBF), after further acid (5% HCl, 30%  $\text{HNO}_3$ ) and heat treatments (5 M NaOH solution, 60 °C, 24 h). However, the adhesion of the Ti layers was insufficient.<sup>[40]</sup> A two-step procedure was developed with first electrochemical-hydrothermal treatment of the Ti-BMG in 5 M NaOH solution (90 °C, 1 h, 10 mA  $\text{cm}^{-2}$ ) and a subsequent treatment in

saturated  $\text{Na}_2\text{HPO}_4$  and  $\text{Ca}(\text{OH})_2$  (25 °C, 4 h) which resulted in accelerated nucleation and growth rates of apatite formation in SBF.<sup>[41]</sup> Nonetheless, these complex treatments are costly and time-consuming. For Cu-containing glassy Ti-alloys, typical implant oxidation techniques for surface bioactivation based on anodization in suitable electrolytes at high voltages, e.g., oxide nanotubular growth or microporous oxide generation<sup>[42,43]</sup> are expected to be unsuccessful as Cu disturbs the high field-controlled oxide growth processes which are driven by valve-metal properties. In addition, BMG surface thermal oxidation is strongly restricted to a temperature–time window below the supercooled liquid region to suppress crystallization processes.<sup>[44]</sup> Likewise, classical acid etching treatments in HF or HCl solutions are not applicable since they will enhance Cu at the surface, thus inducing local corrosion and diminishing the mechanical performance.<sup>[45,46]</sup>

For the stimulation of bone tissue forming cells, nanostructured implant surfaces with an oxidic nature are most suitable.<sup>[47]</sup> To achieve tailored nanoporous structures and a substantial reduction of Cu species in the near-surface Ti–Cu-based BMG region, techniques adapted from dealloying emerge promising. This process was fundamentally developed for crystalline noble metal alloys in a single solution state. By chemical or electrochemical treatments, a selective dissolution of the less noble constituent species occurs, followed by surface diffusion of the remaining more noble constituent atoms, thereby rearranging to nanosized ligaments which create three-dimensional (3D) networks with open nanoporosity.<sup>[48,49]</sup> As prerequisite, the dissolving less noble constituent has to be in excess concentration in the alloy substrate. In initial studies, chemical dealloying processes for single-phase amorphous alloys based on complex noble metal-based systems were investigated. For instance, Paschalidou et al. achieved full dealloying of glassy  $\text{Au}_{40}\text{Cu}_{28}\text{Ag}_7\text{Pd}_5\text{Si}_{20}$  ribbons resulting in homogeneous nanoporous gold (Au) by immersion in 1 M  $\text{HNO}_3$  solution at 70 °C.<sup>[50]</sup> However, in the case of valve metal-based alloys, such selective surface processes are extremely difficult, as the atomic surface diffusion and reorganization processes of the remaining components are partially or completely inhibited by immediate oxidation. Thus, the penetration depth of the dealloying process is limited. Exemplarily, L. Mihaylov et al. treated the surfaces of glassy  $\text{Zr}_{65}\text{Ni}_{30}\text{Pd}_5$  and  $\text{Zr}_{55}\text{Ni}_{30}\text{Al}_{10}\text{Pd}_5$  alloy ribbons in 0.01 M HF solution for 24 h and obtained a nanoporous layer with a limited thickness of 2–3  $\mu\text{m}$  which was composed of nanocrystalline Pd, ZrNi,  $\text{ZrO}_2$ , and NiO.<sup>[51]</sup> Due to these limitations, the process cannot be referred to as dealloying per definition. Consequently, the terminology “pseudo-dealloying” is introduced in this article to describe the surface nanostructuring process occurring in the Ti–Cu-based glassy alloy.

For removing Cu from the near-surface regions of the glassy alloy, the chemical process has to be conducted in the pH value-potential regimes at which soluble Cu species can form, i.e., in strongly acidic or alkaline solutions and under oxidizing (anodic) conditions in the water stability range, which also enhances the Ti (and Zr or Nb oxidation).<sup>[52]</sup> In the first study, Blanquer et al. obtained by potentiodynamic polarization of glassy  $\text{Ti}_{40}\text{Zr}_{10}\text{Cu}_{38}\text{Pd}_{12}$  bulk samples in 5 M NaOH solution a nanoporous mesh layer with 200 nm thickness which was described as being rich in Ti and Cu oxides and Pd, i.e., Cu

was only reduced by about half the amount compared to the content in the glassy alloy matrix.<sup>[53]</sup>

In this article, we describe the first successful steps to develop a suitable approach for the formation of a nanoporous Ti-oxide-based layer on glassy  $\text{Ti}_{47}\text{Cu}_{38}\text{Fe}_{2.5}\text{Zr}_{7.5}\text{Sn}_2\text{Si}_1\text{Ag}_2$  ribbon samples by electrochemical pseudo-dealloying in nitric acid solution ( $\text{HNO}_3$ ) at elevated temperatures. It will be demonstrated that, the applied anodic potential controls the surface reactions which take place in three characteristic stages, thereby leading to porous surface layers with ligament and pore sizes in the range of a few nanometers. These porous oxide layers can effectively suppress pitting corrosion in a simulated physiological solution leading to cp-Ti-like good corrosion resistance.

## 2. Experimental Section

### 2.1. Preparation of Glassy Alloy Samples

For these fundamental electrochemical surface treatment studies, ribbon samples of the  $\text{Ti}_{47}\text{Cu}_{38}\text{Fe}_{2.5}\text{Zr}_{7.5}\text{Sn}_2\text{Si}_1\text{Ag}_2$  alloy were fabricated by melt-spinning and used as free-standing working electrodes with a large surface area.

For the alloy fabrication, all commercial constituent elements with a purity higher than 99.99% were mechanically cleaned using grinding SiC paper to remove surface oxides and impurities and subsequently, were mixed in appropriate concentrations. Ingots with a targeted composition of  $\text{Ti}_{47}\text{Cu}_{38}\text{Fe}_{2.5}\text{Zr}_{7.5}\text{Sn}_2\text{Si}_1\text{Ag}_2$  and a weight of 25 g were prepared by arc melting (Edmund Bühler GmbH) in a Ti-gettered argon atmosphere. Each ingot was remelted at least five times to ensure chemical homogeneity. Pieces of the master alloy (5–6 g) were used to produce ribbons with a width of 4–5 mm and a thickness of about 30–50  $\mu\text{m}$  in a Cu single-roller melt spinner, with a diameter of 0.20 m (Edmund Bühler GmbH). The casting temperature was 1076 K. The tangential speed of the copper wheel was 41  $\text{m s}^{-1}$  for all the ribbons.

### 2.2. Characterization of the Master Alloy and Glassy Ribbons

The elemental composition of the produced master alloy and glassy ribbons was examined by inductively coupled plasma optical emission spectroscopy (ICP-OES; iCAP 6500 Duo View, Thermo Fisher Scientific GmbH). The obtained results are listed in Table 1. Considering the error limits of the analysis method, the compositional deviations are negligible; thus, the material will be denoted by its nominal composition (in at%).

The oxygen content was determined by the carrier gas hot extraction method (CGHE; LECO ON836, LECO Corporation). The measured oxygen levels are low, i.e., 0.073 ( $\pm 0.015$ ) wt%

for ribbons and 0.0651 ( $\pm 0.0025$ ) wt% for the master alloy, hence proving the high purity of the produced materials.

The microstructure of the as-spun alloy was examined by X-ray diffraction (XRD; STOE Stadi P) in transmission geometry mode using  $\text{Mo K}_{\alpha 1}$  ( $\lambda = 0.70930 \text{ \AA}$ ) monochromatic radiation and  $0.5^\circ$  step size. The thermal stability and crystallization behaviors were studied by differential scanning calorimetry (DSC; Perkin-Elmer DSC7) at a heating rate of  $0.33 \text{ K s}^{-1}$  in an  $\text{Al}_2\text{O}_3$  pan. A thermal relaxation step, i.e., preheating up to 673 K, was added to the DSC measurements to determine a more reliable glass-transition temperature,  $T_g$ . From the onset temperatures of  $T_g$  and the first crystallization peak ( $T_x$ ), the undercooled liquid region ( $\Delta T_x$ ) was determined.

### 2.3. Surface Modification by Electrochemical Treatment in Nitric Acid and Surface Analysis

Electrochemical pseudo-dealloying was applied to modify the surface of the glassy  $\text{Ti}_{47}\text{Cu}_{38}\text{Fe}_{2.5}\text{Zr}_{7.5}\text{Sn}_2\text{Si}_1\text{Ag}_2$  ribbons. Electrochemical tests were carried out using a Solartron SI 1287 electrochemical interface connected to a three-electrode biological cell with a double-wall jacket for temperature control (BioLogic). A saturated calomel electrode (SCE) ( $E(\text{SHE}) = 0.241 \text{ V}$ ) was used as the external reference electrode with a Luggin capillary. A Pt sheet served as a counter electrode. As a working electrode, 3–4 cm long ribbon pieces were cut, electrically connected at one end, and partially isolated with Teflon tape exposing an area of  $1 \text{ cm}^2$ . Measurements were conducted at room temperature (RT) and at  $60^\circ \text{C}$  in 5 M  $\text{HNO}_3$  solution (65% p.a., CHEMSOLUTE). These electrolyte conditions (pH value and concentration) for the surface modification were selected considering the Pourbaix diagrams of Ti (hydrous and anhydrous) and Cu at  $25^\circ \text{C}$ ,<sup>[52]</sup> as well as the work of Zhu et al. for binary Ti–Cu alloys with excess of Cu content.<sup>[54,55]</sup>

After pre-exposure of the ribbon sample for 30 min under open circuit potential (OCP) conditions, linear potentiodynamic polarization measurements in 5 M  $\text{HNO}_3$  solution in the range  $-0.2 \text{ V}$  versus OCP to  $2 \text{ V}$  (vs SCE) with a potential scan rate of  $1 \text{ mV s}^{-1}$  were carried out. This was done to determine the suitable conditions for potentiostatic pseudo-dealloying. After immersion of the ribbons for 10 min under OCP conditions, the potential was set to a defined anodic potential and was held constant for 60 min while the current transient was recorded. To evaluate the influence on the resulting surface nanostructure, different potentials in the pseudo-passive and transpassive regions were applied. After the electrochemical treatment, the samples were rinsed four times with distilled water and were left to dry at RT. All tests have been repeated at least 3 times to ensure the reliability of the data. The air side of the ribbon was used for surface analysis.

**Table 1.** ICP-OES results—measured chemical compositions for alloy samples made of nominal  $\text{Ti}_{47}\text{Cu}_{38}\text{Fe}_{2.5}\text{Zr}_{7.5}\text{Sn}_2\text{Si}_1\text{Ag}_2$ .

	Element content [at%]						
	Ti	Cu	Zr	Fe	Sn	Si	Ag
Master alloy	47.23 $\pm$ 0.26	37.91 $\pm$ 0.07	7.45 $\pm$ 0.21	2.08 $\pm$ 0.01	1.97 $\pm$ 0.01	0.84 $\pm$ 0.01	2.00 $\pm$ 0.01
Ribbons	47.03 $\pm$ 0.37	38.04 $\pm$ 0.22	7.48 $\pm$ 0.22	2.11 $\pm$ 0.06	1.99 $\pm$ 0.03	0.97 $\pm$ 0.06	1.99 $\pm$ 0.05

## 2.4. Surface Characterization

The surface morphology of the nontreated and treated samples was investigated by field emission scanning electron microscope (FE-SEM; Zeiss Ultra Plus) with an energy of 20 keV. Lamella cross-sections were prepared using a focused ion beam (FIB; Thermo Fisher Helios 6000) and examined with transmission electron microscopy (TEM; Thermo Fisher Tecnai G20) operating at 200 kV to determine the thickness of the oxide layer. Images were taken using underfocus conditions. Image-J software was used on 50 spots in SEM images from 3 different sample replicates at each investigated potential to determine the pore and ligament sizes.

For the characterization of the nontreated and treated surface of the glassy ribbons (airside), chemical depth profiles were obtained using Auger electron spectroscopy (AES) in combination with Argon ion etching. The spectrometer (JEOL JAMP 9500F) is equipped with a hemispherical analyzer and operates with the electron beam conditions: 10 kV, 10 nA. The Argon ions are accelerated with 1 kV leading to an estimated sputter rate of  $6 \text{ nm min}^{-1}$  (calibrated to  $\text{SiO}_2$ ). The sputter spot size of approximately  $1 \text{ mm} \times 1 \text{ mm}$  is some orders of magnitude higher than the analyzing areas. At least two spots per surface sample were analyzed.

The surface/bulk interface was set at the point where the oxygen concentration was at 50% of its maximum.

Normalized  $\text{Cu}/(\text{Ti} + \text{Zr})$  values were obtained by first finding the ratio of atomic concentrations of Cu to the sum of the atomic concentrations of Ti and Zr ( $\text{Ti} + \text{Zr}$ ) and then driving the calculated ratio values to the highest value of  $\text{Cu}/(\text{Ti} + \text{Zr})$  in the as-spun sample.

For a better understanding of the binding states at the surface, X-ray photoelectron spectroscopy (XPS) is used. The spectrometer (Physical Electronics PHI 5600) is equipped with a 150 mm hemispherical analyzer and a monochromated  $\text{Al-K}\alpha$  X-ray source. High-resolution spectra were obtained with a 29 eV pass energy and a 0.8 mm spot size. A low-energy electron gun (5 V) is used as a neutralizer to avoid any kind of surface changing during the measurement. All spectra are energy-corrected using graphitic carbon at 284.4 eV as a reference.

Atomic force microscopy (AFM) was performed under ambient conditions using a Bruker Dimension Icon AFM in tapping mode with a scan rate of 0.5 Hz. A TESPA-v2 probe was used with a resonance frequency of 320 kHz. The AFM data were analyzed using WSxM5.0 Develop 10.0 and/or Gwyddion 2.56.

## 2.5. Corrosion Measurements

Electrochemical measurements were carried out in a simulated physiological solution to study the impact of the selected surface treatments on the corrosion properties of the glassy ribbons. Pure Ti in the form of sheets was used as a reference material. To resemble the initial surface conditions of the ribbons, Ti sheets were mechanically ground with 2500 SiC paper and exposed to laboratory ambient conditions for 24 h. In addition, Ti sheets were pre-exposed to 5 M  $\text{HNO}_3$  solution at 60 °C applying a potential of 1 V for 3600 s to stimulate the passivation and making it comparable with the glassy ribbons pre-exposed to the same treatment.

The electrolyte chosen for the measurements was phosphate-buffered saline solution (PBS; composition: NaCl 140 mM, KCl 3 mM, phosphate buffer 10 mM, purchased from Merck KGaA), at 37 °C and pH 7.4. A three-electrode glass cell connected to a Solartron SI 1287 electrochemical interface as described above was used, with the working electrode exposing an area of  $1 \text{ cm}^2$ .

Samples were immersed for 60 min in OCP conditions to monitor the stabilization of the potential. Potentiodynamic polarizations were started at  $-0.2 \text{ V}$  versus OCP and the potential was ramped to 1.2 V versus SCE at a constant scan rate of  $1 \text{ mV s}^{-1}$ . A current density limit of  $1 \text{ mA cm}^{-2}$  was set to interrupt local corrosion processes which typically occur in the anodic regime with a sudden strong current increase. Each test was performed at least three times to ensure the repeatability of the results. The corrosion parameters, corrosion potential ( $E_{\text{corr}}$ ), corrosion current density ( $i_{\text{corr}}$ ), and passive current density ( $i_{\text{pass}}$ ) at 1 V versus SCE were determined by graphical extrapolation from the representation of the polarization curves.

After these tests, the sample surfaces were examined with SEM to analyze possible corrosion damage morphologies.

## 3. Results and Discussion

### 3.1. Characterization of $\text{Ti}_{47}\text{Cu}_{38}\text{Fe}_{2.5}\text{Zr}_{7.5}\text{Sn}_2\text{Si}_1\text{Ag}_2$ Ribbon Material

To conduct fundamental electrochemical surface treatment investigations, ribbon samples were produced from a  $\text{Ti}_{47}\text{Cu}_{38}\text{Fe}_{2.5}\text{Zr}_{7.5}\text{Sn}_2\text{Si}_1\text{Ag}_2$  alloy using melt spinning. These ribbons served as independent working electrodes with a large surface area, making them highly suitable for in-depth surface analytical research.

To characterize the microstructure and the thermal properties of the as-spun ribbons, DSC and XRD investigations were performed. The DSC scan in **Figure 1** confirms the glassy nature of the ribbon. Upon heating (after a preheating for structural relaxation), an endothermic event sets in at  $T_g$  (onset) =  $645 \pm 2 \text{ K}$ , which can be attributed to the glass transition to the undercooled liquid. Subsequently, a crystallization event is observed starting at  $T_{x1}$  (onset) =  $701 \pm 2 \text{ K}$ . From these temperatures, an undercooled liquid region of  $\Delta T_x = 56 \pm 2 \text{ K}$  is derived. These results are similar to those reported in earlier literature for this BMG composition, i.e., for ribbons and cast rods measured with the same heating rate.<sup>[14]</sup> Upon further heating, a second main crystallization event occurs with a main exothermic peak ( $T_{x2}$  (onset) =  $809 \pm 1 \text{ K}$ ) accompanied by two characteristic shoulders, similar to what was observed in the literature,<sup>[14]</sup> indicating a complex thermal crystallization scheme of the glassy alloy. An exemplary XRD pattern of the  $\text{Ti}_{47}\text{Cu}_{38}\text{Zr}_{7.5}\text{Fe}_{2.5}\text{Sn}_2\text{Si}_1\text{Ag}_2$  glassy ribbon is shown in the inset in **Figure 1**. The broad peaks on the wheel and airside indicate that the ribbon is amorphous, and the lack of sharp reflections reveals the nonexistence of crystalline side phases.

In general, from the thermal analysis it can be concluded, that this metallic glass is very stable, and therefore, the subsequent electrochemical treatments at 60 °C will not affect the alloy substrate state.

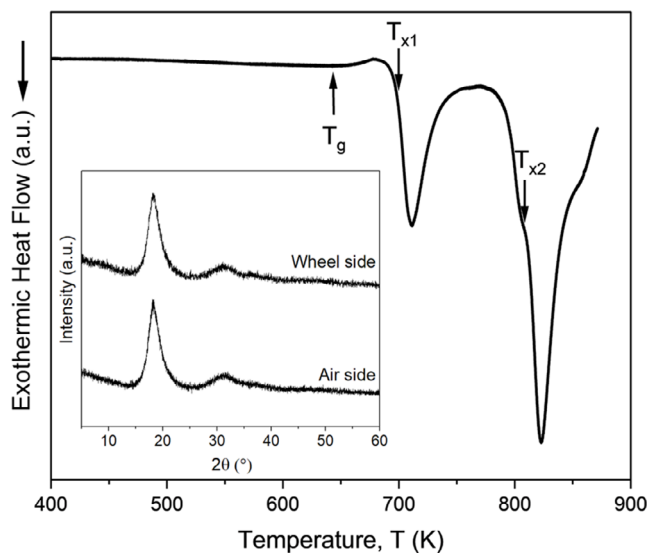


**Figure 1.** DSC curve recorded with a heating rate of  $0.33 \text{ K s}^{-1}$ , after structural relaxation preheating up to 673 K with inset XRD pattern measured in the transmission mode of a  $\text{Ti}_{47}\text{Cu}_{38}\text{Zr}_{7.5}\text{Fe}_{2.5}\text{Sn}_2\text{Si}_1\text{Ag}_2$  ribbon material wheel and airside.

### 3.2. Surface Modification by Electrochemical Pseudo-Dealloying

#### 3.2.1. Potentiodynamic Polarization of Glassy

##### $\text{Ti}_{47}\text{Cu}_{38}\text{Zr}_{7.5}\text{Fe}_{2.5}\text{Sn}_2\text{Si}_1\text{Ag}_2$ in 5 M $\text{HNO}_3$ Solution

In the first step, the electrochemical reactivity of the glassy  $\text{Ti}_{47}\text{Cu}_{38}\text{Zr}_{7.5}\text{Fe}_{2.5}\text{Sn}_2\text{Si}_1\text{Ag}_2$  alloy was generally assessed. Potentiodynamic polarization curves of the ribbon samples in 5 M  $\text{HNO}_3$  solution at RT and  $60^\circ\text{C}$  are shown in **Figure 2**, these were recorded after 30 min of OCP stabilization (inset). The OCP at both conditions manifests a characteristic initial behavior. In the case of the one recorded at RT, there is an increase of potential over time, thus exposing the formation of a passive film. For the one at  $60^\circ\text{C}$ , there is a decay of potential over time, which is linked to the surface activation of the alloy.

Potentiodynamic polarization curves at RT show the typical behavior of an air-aged Ti-based metallic glass sample with low corrosion reactivity and stable anodic passivity. This translates into a very low corrosion current density ( $i_{\text{corr}} < 1 \times 10^{-7} \text{ A cm}^{-2}$ ) and a gradual anodic transformation to a current density plateau of about  $2 \times 10^{-5} \text{ A cm}^{-2}$ , before reaching the water decomposition regime. Despite  $\text{HNO}_3$  being known for selectively dissolving Cu,<sup>[54,55]</sup> the high corrosion resistance in the concentrated electrolyte also suggests that these are not the appropriate conditions to induce selective surface dissolution processes. According to the Cu- $\text{H}_2\text{O}$  (at  $25^\circ\text{C}$ ) potential-pH value diagram,<sup>[52]</sup> Cu dissolution can be expected from the beginning of the anodic regime. Nonetheless, the rapid and strong passivating nature of the valve metal constituents, Ti and Zr, suppresses this process. This fact was earlier discussed in detail for Zr-based glasses.<sup>[3,56,57]</sup>

However, when increasing the electrolyte temperature to  $60^\circ\text{C}$ , the electrochemical activity of the glassy alloy, as well as the Cu selective dissolution and the formation of the passive layer, are significantly enhanced. The corrosion current density

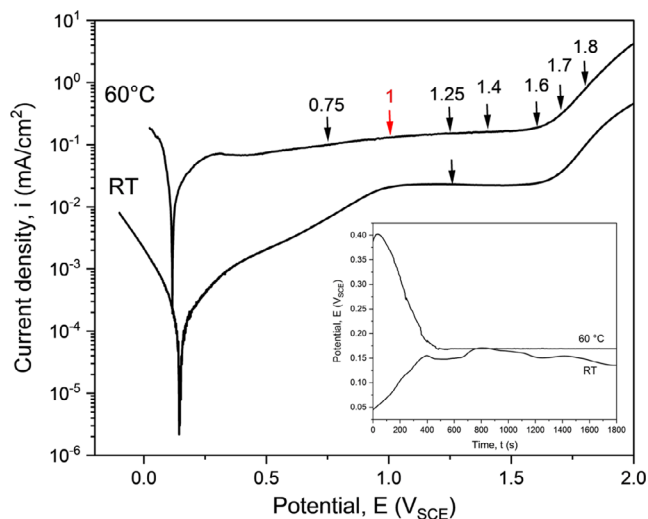


**Figure 2.** Potentiodynamic polarization curves of glassy  $\text{Ti}_{47}\text{Cu}_{38}\text{Zr}_{7.5}\text{Fe}_{2.5}\text{Sn}_2\text{Si}_1\text{Ag}_2$  alloy samples in 5 M  $\text{HNO}_3$  solution at RT and  $60^\circ\text{C}$ , measured with a potential scan rate of  $1 \text{ mV s}^{-1}$ . The arrows indicate anodic potentials which were selected for further potentiostatic studies; inset: previous OCP stabilization at RT and  $60^\circ\text{C}$ .

( $i_{\text{corr}}$ ) is increased by two orders of magnitude reaching a value of  $1 \times 10^{-5} \text{ A cm}^{-2}$  and the corresponding corrosion potential ( $E_{\text{corr}}$ ) is shifted in the negative direction by about 30 mV compared to the RT value. This free corrosion enhancement is due to both accelerated anodic and cathodic partial reactions. Upon anodic polarization, a direct transition into a current density plateau region without a significant active-passive peak is observed. In the plateau regime, the current density increases only gradually from  $1 \times 10^{-4} \text{ A cm}^{-2}$  at 0.75 V versus SCE to  $1.8 \times 10^{-4} \text{ A cm}^{-2}$  at 1.6 V versus SCE. These values are about one order of magnitude higher than those measured at RT, but still account for a passive behavior with higher oxide film permeability. Therefore, we define this as a “pseudo-passive” state. At potentials higher than 1.6 V versus SCE, a steep current density increase occurs, which indicates a transpassive regime where alloy surface oxidation is superimposed by water decomposition.

Since in pretests (Figure S1, Supporting Information), no substantial surface changes were observed when operating at RT, the elevated temperature conditions were considered a critical and decisive factor for the expected anodic pseudo-dealloying to occur.

These polarization curves were used to identify the appropriate conditions for further studying potentiostatic pseudo-dealloying. Different potentials, indicated in Figure 2 by arrows, were selected within the pseudo-passive and the transpassive regime at  $60^\circ\text{C}$  to analyze the effect they had on the morphology, thickness, and composition of the developing surface layers.

#### 3.2.2. Potentiostatic Polarization of Glassy

##### $\text{Ti}_{47}\text{Cu}_{38}\text{Zr}_{7.5}\text{Fe}_{2.5}\text{Sn}_2\text{Si}_1\text{Ag}_2$ at 1 V versus SCE in $60^\circ\text{C}$ 5 M $\text{HNO}_3$ Solution

In a potentiostatic polarization experiment using 5 M  $\text{HNO}_3$  solution at  $60^\circ\text{C}$ , the potential of the glassy working electrode was

stepped from an OCP value reached after 10 min to a selected potential in the anodic regime (derived from Figure 2).

Exemplary, a double logarithmic current density versus time dependence (current transient, log–log plot) curve, as response to the applied potential of 1 V versus SCE in the pseudo-passive region is shown in **Figure 3**. This is used as a reference to clarify the mechanism involving the electrochemical pseudo-dealloying process. The transient curve has a characteristic shape in which three different regions can be distinguished. Region I exhibits an initial strong decay of the current density up to about 50 s. This performance is typical for a passive film growth based on Ti- and Zr-based metallic glass surfaces. Such behavior at RT (and in this case for the treatment performed at 60 °C) with nearly exponential decay was ascribed to a predominantly high-field oxide growth mechanism, which is typical for valve metals, here, Ti and Zr. This fast selective-element oxidation yields an accumulation of Cu species (and maybe other minor constituent species) in near-surface regions.<sup>[3,56,57]</sup> Region II commencing from 50 to 350 s is characterized by a small peak of the current density. It is assumed that a temporary breakdown of the passive film occurs, thus allowing surface dissolution, i.e., mainly of Cu species from the enriched subsurface region.<sup>[56]</sup> Finally, in region III the transient reaches a nearly plateau-like region with a low current density level of about  $6 \times 10^{-5} \text{ A cm}^{-2}$  at about 350 s and with a gradual increase to about  $8 \times 10^{-5} \text{ A cm}^{-2}$  at 3600 s which is likely due to further growth of oxide films on the alloy surface. The results from different complementing characterization techniques are presented below as supporting evidence for the occurrence of these processes for each region. Glassy samples were polarized at a potential of 1 V versus SCE up to an end time point of a respective transient region and then, the air ribbon sides were subjected to surface analytical studies using FE-SEM and AES chemical depth profiling, as shown in Figure 3 and 4. For that, electrochemical experiments were stopped after 40 s (region I), 300 s (region II), and 3600 s (region III) of

applying potential. The surface of a ribbon sample corresponding to region I did not show any distinct features compared to that of the as-spun state, indicating a similarly very smooth surface. On the contrary, in the case of the sample for which the polarization was stopped at region II, the first weak features of surface nano-roughness can be appreciated. While in the case of region III, the pronounced formation of a nanoporous structure, with characteristic pores and ligaments, is evident.

An XRD pattern in transmission mode corresponding to region III confirmed the amorphous nature of the ribbon sample after the pseudo-dealloying process (Figure S2, Supporting Information).

Moreover, samples were subjected to AES analysis with sputter depth profiling to obtain the chemical composition information in near-surface regions. Only the main constituents of the  $\text{Ti}_{47}\text{Cu}_{38}\text{Zr}_{7.5}\text{Fe}_{2.5}\text{Sn}_2\text{Si}_1\text{Ag}_2$  alloy, namely, Ti, Zr, and Cu, as well as oxygen (O) were considered, while the other minor constituents remained below the detection limit. Representative depth profiles of alloy surfaces, which were polarized at 1 V versus SCE in 5 M  $\text{HNO}_3$  solution to different endpoints and of the as-spun surface state are shown in **Figure 4**.

In general, the profiles here show initially high concentrations of oxygen, which decay with increasing sputter times. Whereas, the major metallic component Ti starts at minimum concentrations, which then correspondingly increase. These profile trends indicate the presence of an oxide layer at the surface. In such cases, the half value of the maxima and minima plateaus of the O profile can be considered the oxide/bulk interface region.<sup>[56]</sup>

In Figure 4a, the as-spun surface reveals an oxide region with approximately 8 nm thickness, as derived from the O profile (considering a standard sputter rate in  $\text{SiO}_2$  of  $6 \text{ nm min}^{-1}$ ). The formation of these films, which are mainly composed of Ti-oxide species, is attributable to spontaneous passivation during storage under ambient conditions (air-aging). Further, a

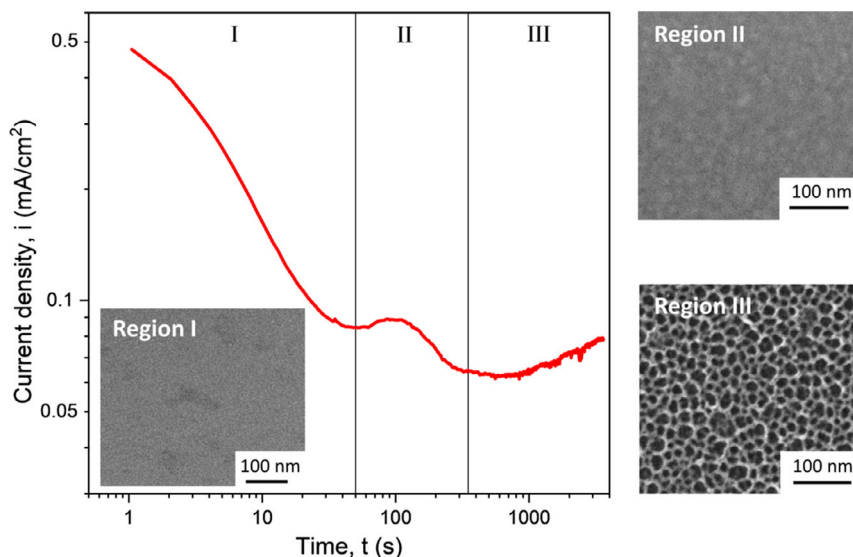


**Figure 3.** Current density transient (log–log plot) of a glassy  $\text{Ti}_{47}\text{Cu}_{38}\text{Zr}_{7.5}\text{Fe}_{2.5}\text{Sn}_2\text{Si}_1\text{Ag}_2$  alloy sample recorded during potentiostatic polarization at 1 V versus SCE in 5 M  $\text{HNO}_3$  at 60 °C and FE-SEM images of ribbon surfaces (airside) taken after polarization different time points of the three characteristic regions: after 40 s (region I), 300 s (region II), and 3600 s (region III).

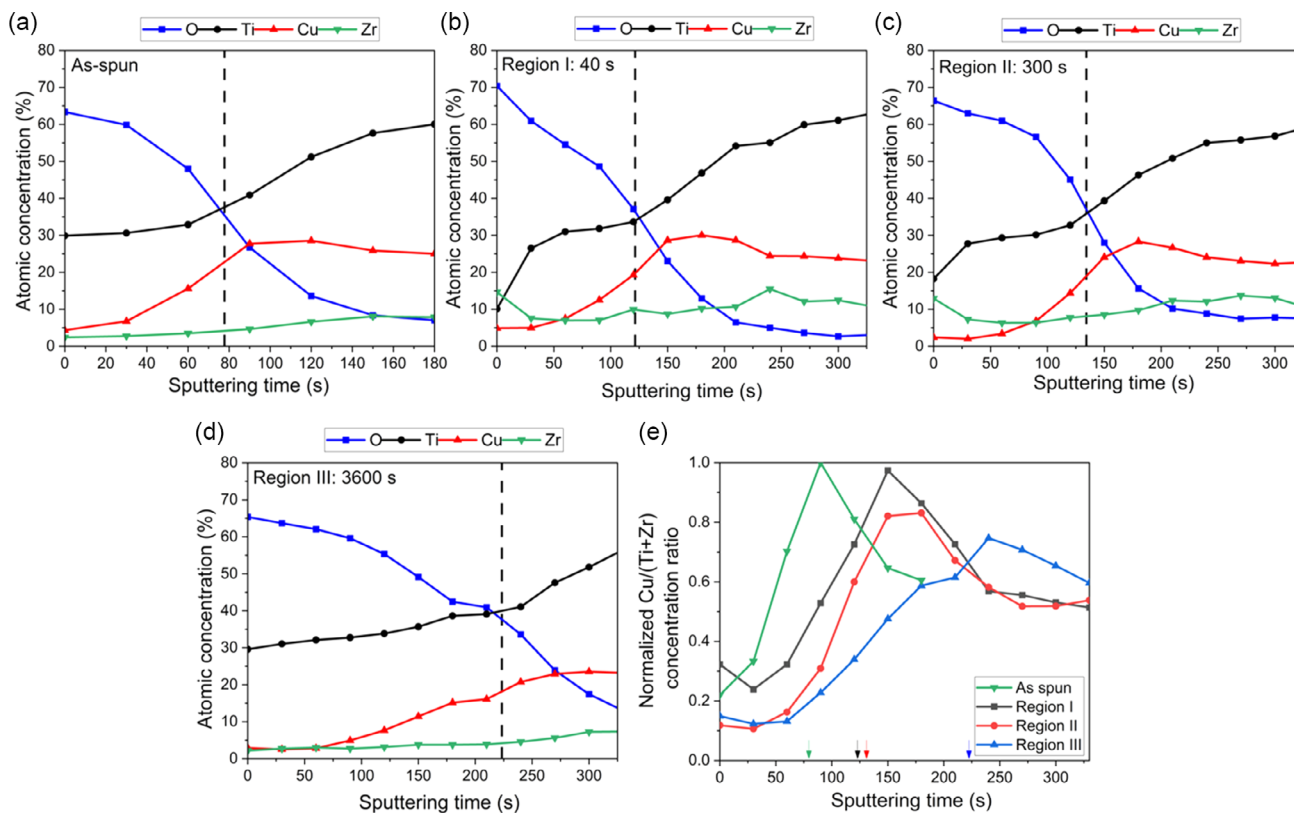


**Figure 4.** a) AES chemical depth profiles considering Ti, Zr, Cu, and O of the as-spun (air-aged) state, after polarization: b) after 40 s (region I), c) 300 s (region II), d) 3600 s (region III), and e) normalized Cu/(Ti+Zr) ratios of surface states of the glassy  $\text{Ti}_{47}\text{Cu}_{38}\text{Zr}_{7.5}\text{Fe}_{2.5}\text{Sn}_2\text{Si}_1\text{Ag}_2$  alloy (air ribbon side) derived from the profiles in (a–d). Dashed vertical lines (a–d) and colored arrows (e) indicate the depth extent of the oxide film, derived from the oxygen profile and a sputter rate of  $6 \text{ nm min}^{-1}$ : (a) 8 nm, (b) 12 nm, (c) 14 nm, and (d) 22 nm.

slight enrichment of Cu near the oxide/metal interface can be seen, analogous to reported results for Zr–Cu-based BMGs in as-prepared passivated state due to the selective oxidation of the valve metal constituents.<sup>[56,57]</sup>

Note that the atomic concentrations of the main constituents in the alloy substrate region strongly deviate from the nominal bulk composition of the alloy (confirmed by ICP-OES). Besides, the exclusion of the minor alloy constituents from the analysis, this is attributable to measurement uncertainties inherent to the technique and sputtering effects.<sup>[58]</sup> Nevertheless, under similar experimental conditions, near-surface regions can be compared to determine significant differences.

After electrochemical treatment until the end of region I in the transient (in Figure 4b), the oxide film thickness further increased slightly, i.e., up to 12 nm. Here, Ti species, as well as Zr species, are present in the outermost regions, while Cu enrichment near the oxide/bulk interface is slightly more pronounced (note the different sputtering time scales). This confirms that, in the first decaying region of the current density transient, predominantly a further passive film growth of mainly Ti and Zr occurs.

For alloy samples exposed for longer times to the potentiostatic treatment at 1 V versus SCE, thicker oxide film regions are detectable, i.e., about 14 nm after transient region II (300 s) in Figure 4c, and about 22 nm after region III (3600 s) in

Figure 4d. Owing to the nanoporous oxide film nature generated in region III (SEM image, Figure 3), the depth profile for oxygen is less steep, but the film mainly comprises of Ti-species. In addition, the Cu maximum in the depth profiles is apparently lower and is shifted to longer sputtering times.

The changes in the relative concentrations of Cu across the depth profile for each specimen could be more clearly appreciated by plotting the ratio of the Cu concentrations to the amount of the main metallic elements of the oxide layer (Ti and Zr),  $\text{Cu}/(\text{Ti} + \text{Zr})$ , against the sputtering time (Figure 4e). To more effectively see the difference among the samples, the values were also normalized to the highest  $\text{Cu}/(\text{Ti} + \text{Zr})$  value in the as-spun sample. In Figure 4e, increasing oxide thickness (based on the increasing sputtering time), corresponding to the oxide/bulk interface (arrows) starting from the as-spun (representing the air-aging oxide) to increasing potentiostatic polarization times (increasing from region I to region III), can be observed. First, the effect of the electrochemical treatment in growing the oxide even for a short time of 40 s can be noticed, clearly showing the fast oxidation process occurring in region I of the transient. Then, at region II, the passive film breakdown temporarily occurs simultaneously with the oxidation, leading to a small increase in the thickness. At region III, continuous passive film growth occurs gradually, and after 3600 s, a thicker oxide is obtained. This occurs at a slower rate than the oxidation at region

I such that after 3600 s ( $90 \times 40$  s), the thickness increase is less than twice the size of the thickness obtained with the fast oxidation process.

The values of the normalized Cu/(Ti + Zr) ratios further emphasize the Cu enrichment near the oxide/bulk interface, distinctly showing the maximum in the curves, which decreases as the electrochemical treatment progresses (i.e., as-spun (air-aged) > region I > region II > region III). A high ratio value, almost similar to that of the as-spun sample for the region I curve, matches the accumulation of the Cu species occurring near the interface (green arrow) which would be expected due to the fast selective-oxidation process. The Cu dissolution occurring in region II results in a lowered (by  $\approx 15\%$  compared to region I) ratio value. In region III, the selective-element oxidation occurs at a slower rate, resulting in a lower Cu accumulation. Possibly, the even lower value is also due to Cu still dissolving. The Cu dissolution however is less likely due to the slower diffusion through the thicker oxide barrier, resulting in a smaller decrease in the value ( $\approx 10\%$  vs region II maximum) than the decrease of the Cu ratio due to the dissolution in region II. As such, considering the lower Cu accumulation due to the slower selective oxidation and likely lower amounts of Cu dissolution, the ratio here is  $\approx 25\%$  less than the as-spun and region I maximum.

XPS analysis was also performed on the surface-near regions of the electrochemically-treated ribbon sample, i.e., at 1 V versus

SCE for 3600 s (end of transient region III), and of the as-spun sample as reference. The detailed spectra for Cu2p, Ti2p, Zr3d, and O1s states are shown in Figure 5.

It is worth mentioning that all the components except Fe were detected but only the relevant ones for this study (Cu, Ti, Zr, and O) are shown.

For the discussion, only the spin-orbit peaks with the highest area ratio, i.e.,  $Ti2p_{3/2}$ ,  $Zr3d_{5/2}$ , and  $Cu2p_{3/2}$ , will be considered. The peaks in  $Ti2p_{1/2}$ ,  $Zr3d_{3/2}$ , and  $Cu2p_{1/2}$  are overlapped and the interpretation of their oxidation states is more intricate. Nonetheless, because of the nature of the splitting, any assumption made from the first peaks will subsequently apply to the second ones.

For Ti2p (Figure 5a), the oxidation state Ti(0) can be detected at 454 eV in both samples. The as-spun sample presents a characteristic peak at 458.8 eV, which corresponds mainly to the contribution of the oxidation state Ti(IV). The treated sample presents the same peaks shifted to a higher binding energy (BE), 459.2 eV. In addition, the presence of Ti(III) at 457.3 eV can be noted in both samples due to the shape asymmetry of the peaks.<sup>[59]</sup> The shift to higher BEs can be attributed to the reduction of the work function of Ti caused by the dissolution of Cu in the near-surface regions due to the electrochemical treatment, changing the environment around Ti.

Regarding the Zr3d spectra (Figure 5b), in both as-spun and treated samples, the presence of Zr(0) can be distinguished by

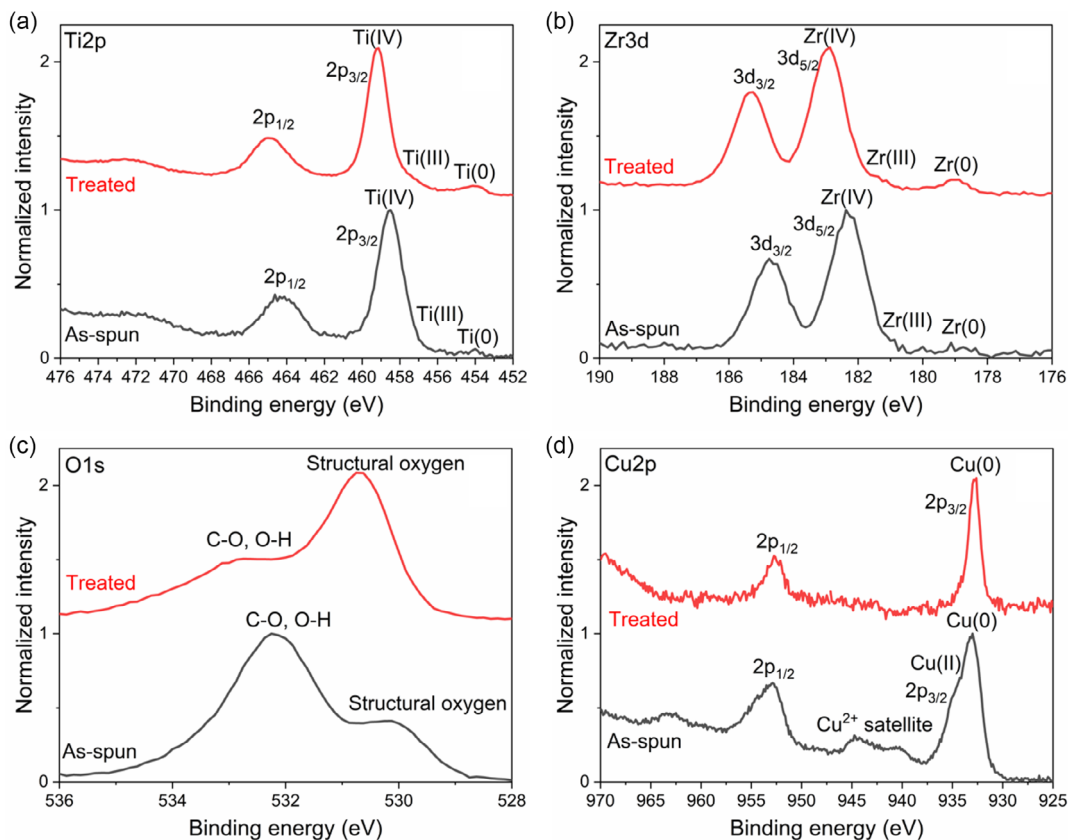


**Figure 5.** XPS analysis considering: a) Ti2p, b) Zr3d, c) O1s, and d) Cu2p surface states of the glassy  $Ti_{47}Cu_{38}Zr_{7.5}Fe_{2.5}Sn_2Si_1Ag_2$  alloy (air ribbon side) after an electrochemical treatment in 5 M  $HNO_3$  60 °C at 1 V versus SCE for 3600 s (treated) and of the as-spun (air-aged) state (as-spun).



the peak presented at 178 eV. The as-spun sample exhibits a distinctive peak at 182.3 eV, which corresponds to the oxidation state Zr(IV). Following the same scenario as Ti2p, the treated sample presents the same peak shifted to a slightly higher BE, 182.9 eV, for the same reason. Also, both samples present peak asymmetry attributed to the presence of Zr(III).

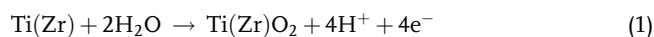
For the O1s spectra (Figure 5c), two main peaks can be differentiated, the so-called structural oxygen at 530 eV corresponding to coordination with Ti(IV) and Zr(IV) (i.e., as nonhydrous oxides) and another at 532–533 eV which can be associated with the presence of hydroxides (coordinated to Cu(II) or to Ti and Zr),<sup>[59,60]</sup> but also possibly due to some organic C-O bonds indicating the presence of carbon in the atmosphere. It can be noticed that in the case of the treated sample, the structural oxygen peak is dominating. This fact can be explained by the thicker oxide layer formed after the electrochemical treatment and the lack of Cu(II) in the oxide film (see below), leaving O atoms more free to coordinate with Ti and Zr. In addition, in the absence of Cu(II) to form hydroxide species (-OH), Ti and Zr can build hydrous oxides.

In the case of Cu2p (Figure 5d), two different oxidation states can be identified. In the as-spun, the main peak appears at 933.1 eV, this value corresponds to the oxidation state Cu(0).<sup>[60]</sup> In addition, a collection of strong satellites in the range of 940–945 eV can be observed. This characteristic feature is attributed to the oxidation state Cu(II), which is likely due to the formation of Cu oxide during air exposure. The shoulder appearing in the peak at 934.8 eV is associated with the presence of hydroxides (and with the corroboration of the strong peak in the O1s spectrum at 532 eV), likely due to the cleaning process. In the case of the treated sample, Cu satellites were not detectable, therefore, the presence of Cu(II) can be ruled out. The defined peak at 932.7 eV can correspond to the oxidation state Cu(0) or Cu(I). With the additional information of the Cu-LMM lines (Figure S3, Supporting Information), it can be deduced that the treated sample presents the oxidation state Cu(0). Altogether, the as-spun sample surface presents a thin oxide film formed by air-aging with the main presence of Ti/Zr(IV) nonhydrous oxides, a mixture of Cu(0) and Cu(II), the latter forming hydroxides (and likely also nonhydrous oxides) and minor presence of Ti/Zr(0) and Ti/Zr(III). Whereas the treated sample exhibits a nanoporous thicker oxide film formed due to the selective Cu(0) oxidation and subsequent dissolution. It also shows a major contribution of Ti/Zr(IV) nonhydrous oxides due to the growth of the film and minor presence of Ti/Zr(0) and Ti/Zr hydrous oxides due to the spontaneous and succeeding reactions with HNO<sub>3</sub>. It is worth mentioning that the presence of Cu is only in its metallic state in the oxide film. This could possibly mean that Cu is in the alloyed form, i.e., coordinated to other metallic species such as Ti, Zr, and/or another Cu. Since the growth of the oxide film and its nanoporous state forming ligaments requires a rearrangement of the structure, it is likely that at some point Ti and/or Zr oxides are not coordinated to O or OH but instead to Cu (and the other metallic species). Such occurrence could, therefore, result in Cu being confined within the alloy unit, preventing its further oxidation and dissolution.

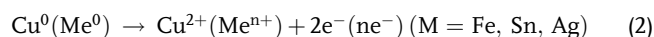
In the results of SEM, TEM, AES, and XPS surface characterization of as-spun and electrochemical treated states and fusing

the Pourbaix diagrams (calculated at RT),<sup>[52]</sup> the following fundamental reaction scheme occurring on the electrode surface during the pseudo-dealloying process in 5 M HNO<sub>3</sub> at 60 °C is presented.

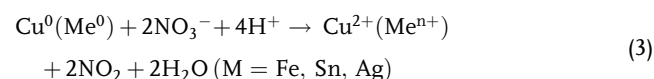
In region I of the current transient (Figure 3) and agree with the corresponding AES measurements (Figure 4b), initial surface state transformation processes include rapid and short passive film formation. Here, a thin barrier-type Ti- and Zr-oxide film (12 nm) with Cu (and minor species) accumulation in the near-surface region is formed following reaction:



Local film breakdown allows Cu (and minor species) dissolution in the near-surface regions in region II of the transient, governed by the reaction:

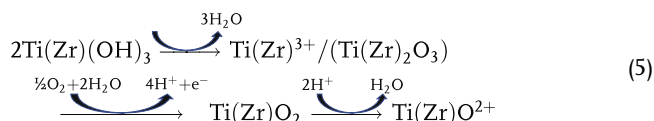
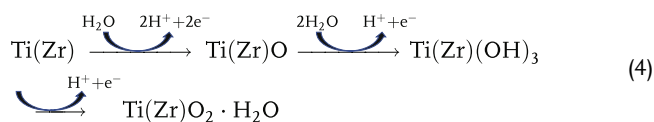


Since it is in a very aggressive environment, the above-listed elements can dissolve even without anodic polarization (but requiring longer times), therefore the following reaction is also contributing to the dissolution:



The growth of the oxide layer is simultaneously taking place, as demonstrated in AES but to a minor degree.

The growth of the oxide layer with a nanoporous morphology in region III is slower compared to that in region I. This is supported by the current transient and AES data, which demonstrate that it took 40 s to form a 12 nm layer and 3600 s to increase the layer to 22 nm in region III (Figure 3 and 4b,d). This is due to the fact that in the course of anodization, the oxide layer undergoes a simultaneous process of thickening and dissolution (Ti(Zr)O<sub>2</sub><sup>+</sup>). This involves the formation of Ti/Zr(III) hydrous oxides, as identified in XPS (Figure 5a,b), under the influence of an aggressive electrolyte. These processes contribute to the development of a porous morphology and topography, as observed in SEM, TEM, and AFM:



Another reason added for the slower growth rate could be the difficulties faced by O and M species in diffusing through the thicker porous oxide film barrier. This fact is also possibly why the Cu accumulation is lower in region III. Further, according to XPS, Cu is trapped in its metallic state. The coordination of Cu with oxidized Ti and Zr atoms prevents its further diffusion, oxidation, and dissolution, inhibiting further pore formation that will expose Ti/Zr(0) to the electrolyte for further oxide formation.

An obstacle of these bulk glass-forming alloy compositions (here  $\text{Ti}_{47}\text{Cu}_{38}\text{Zr}_{7.5}\text{Fe}_{2.5}\text{Sn}_2\text{Si}_1\text{Ag}_2$ ) is that unlike real dealloying processes on metal alloys in solid solution<sup>[48,49]</sup> and as described for binary Ti–Cu alloys with an excess of Cu, like  $\text{Ti}_{40}\text{Cu}_{60}$ ,<sup>[54,55]</sup> the main dissolving species Cu (together with the minor species) are not in excess concentration in the alloy substrate, this also contributes to the strong limitation of the surface reaction progress.

### 3.2.3. Effect of Anodic Potential and Anodization Time on the Nanoporous Layer Growth

In the next step, the influence of different applied anodic potentials on surface transformation reactions of the glassy  $\text{Ti}_{47}\text{Cu}_{38}\text{Zr}_{7.5}\text{Fe}_{2.5}\text{Sn}_2\text{Si}_1\text{Ag}_2$  alloy in 5 M  $\text{HNO}_3$  solution at 60 °C was investigated. According to the potentiodynamic polarization curve presented in Figure 2, specific potentials from the pseudo-passive and from the transpassive region were selected and potential step experiments were conducted. Figure 6 illustrates the corresponding current density transients. At all potentials, the general transient shape is very similar to that described in detail in Section 3.2.2. Especially at potentials in the pseudo-passive regime (0.75–1.6 V vs SCE), the three characteristic regions are clearly visible, indicating that the described surface transformation processes for pseudo-dealloying occur. With increasing potential, the overall current density level increases (as expected). While the slope of the linear regime in region I remains nearly constant, the onset of the Cu peak of region II shifts to earlier times and transforms into a shoulder. Consequently, the onset of region III for nanoporous oxide formation also occurs earlier. These are all indicators for faster potential-driven alloy surface transformation kinetics.

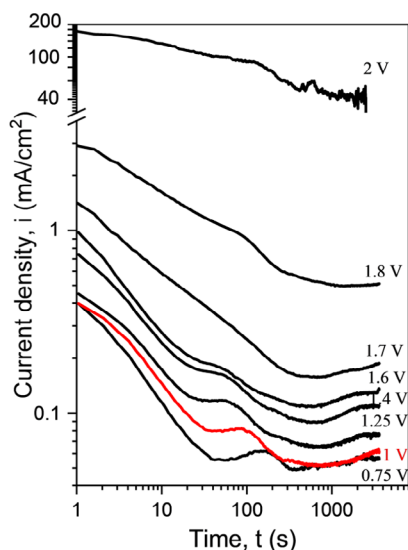


**Figure 6.** Current density transients (log–log plot) of glassy  $\text{Ti}_{47}\text{Cu}_{38}\text{Zr}_{7.5}\text{Fe}_{2.5}\text{Sn}_2\text{Si}_1\text{Ag}_2$  alloy samples recorded during potentiostatic polarization at different potentials in the pseudo-passive and transpassive regions (as indicated in the polarization curve in Figure 2) in 5 M  $\text{HNO}_3$  solution at 60 °C.

At potentials in the transpassive regime, alloy surface oxide formation and dissolution processes are superimposed by the water decomposition reaction with oxygen ( $\text{O}_2$ ) evolution. This explains the substantially higher current density levels of the respective transients in which the initial transformation regions are hardly visible. Despite the fact that oxygen can enhance the alloy surface oxidation by chemical side reactions, it also causes a further local acidification of near-surface electrolyte regions.

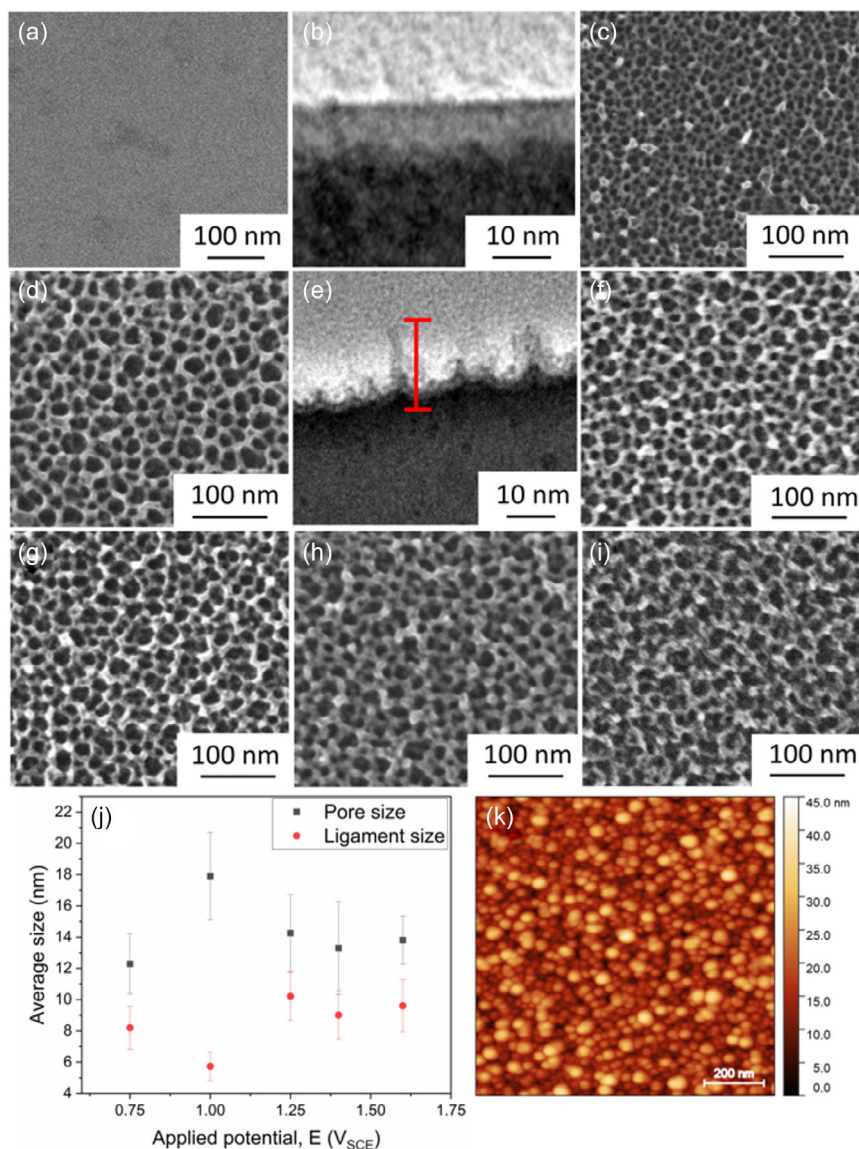
Further, at these elevated potentials, a stronger driving force for the Cu dissolution is given. In the case of an applied potential of 2 V versus SCE, severe surface reactions were expressed by a continuously high current which led to the rupture and degradation of the glassy ribbon sample after less than 900 s of anodization. In the case of binary alloys, Ti–Cu with an excess of Cu content, a potential-dependent surface electropolishing was described under similar electrolyte and polarization conditions.<sup>[54]</sup>

Altogether, this restricts the applicability of the pseudo-dealloying process for the Ti–Cu-based bulk glass-forming alloy to a potential regime of the pseudo-passive and early transpassive state.

After the potential-dependent surface treatments in 5 M  $\text{HNO}_3$  solution at 60 °C for a period of 3600 s, the ribbon surfaces (air side) were comparatively analyzed with FE-SEM and TEM after FIB cutting.

Figure 7 summarizes typical SEM images of the obtained surface states together with that of the initial as-spun state (Figure 7a) as reference. Moreover, a TEM image of the surface cross-section of the as-spun state reveals the presence of the smooth and dense air-formed passive film with thickness below about 10 nm (Figure 7b). All anodically treated samples show the presence of nanoligaments leading to nanopores at their surface. The surface of the samples after each stage of anodization presents a very homogeneous nanoporous morphology with distinct pore and ligament sizes. The treatment at the lowest potential of 0.75 V versus SCE (Figure 7c) resulted in an incomplete nanostructure formation, as seen in the form of small dispersed white artifacts of nonreacted surface areas which are all over the surface. In addition, it has the smallest mean pore size of  $12 \pm 2$  nm, with a ligament size of  $8 \pm 1$  nm. The sample treated under a potential of 1 V versus SCE (Figure 7d) shows the most pronounced structure with the biggest pore size;  $18 \pm 3$  nm and the smallest ligament size;  $6 \pm 1$  nm. A TEM image of the surface cross-section of this sample is provided (Figure 7e). Rounded crevices can be observed in the TEM cross-section corresponding to the formation of the nanopores, and the lighter image contrast in the area following the contour of the crevices indicates the presence of a continuous oxide layer. Remarkably, taller spikes of oxide material, up to 15–20 nm in length, can be observed delimiting the nanopores. The length of the observed oxidic spikes is in good agreement with AES depth profile data (Figure 4).

At higher applied pseudo-passive potentials of 1.25, 1.4, and 1.6 V versus SCE (Figure 7f–h), the nanoporous structure dimensions do not reveal significant changes, showing  $14 \pm 2$ ,  $13 \pm 3$ , and  $14 \pm 3$  nm pore sizes and  $10 \pm 2$ ,  $9 \pm 2$ , and  $10 \pm 2$  nm ligament sizes, respectively.



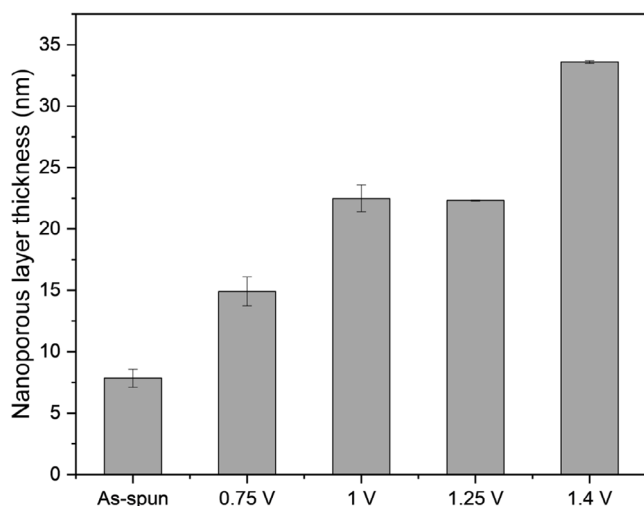
**Figure 7.**  $\text{Ti}_{47}\text{Cu}_{38}\text{Zr}_{7.5}\text{Fe}_{2.5}\text{Sn}_2\text{Si}_1\text{Ag}_2$  glassy ribbon samples (air side): a) SEM image as-spun state, b) TEM FIB cut cross-section as-spun state, SEM images of the potentiostat-treated surfaces at different potentials in 5 M  $\text{HNO}_3$  solution at 60 °C for 3600 s c) 0.75 V, d) 1 V, and e) TEM FIB cut for 1 (thickness indicated in red) V, f) 1.25 V, g) 1.4 V, h) 1.6 V, i) 1.7 V, j) pore and ligament size graph, and k) AFM image of the sample treated at 1.25 V.

Figure 7i shows the nanoporous structure of the sample treated at 1.7 V versus SCE, i.e., relatively close above the transition to the transpassive region (Figure 2), where accelerated surface reactions are expected. This effect is observed in the shape of the ligaments and pores, which in comparison, look more diffuse and not as clearly defined as the samples treated at pseudo-passive potentials. Further, SEM images of sample surfaces obtained at a potential of 1.8 V versus SCE (not shown here) did not show any nanoporous structuring. This confirms the aforementioned statement, in the transpassive regime, the increased anodic current is mainly due to side reactions (water decomposition), triggering alloy surface dissolution rather than the nanoporous oxide formation.

In comparison to the sample treated at 1 V versus SCE, the ligament size has increased while the pore size has been reduced

(Figure 7j). Figure 7k shows an exemplary AFM image taken from a sample surface that was treated at 1.25 V versus SCE. The image analysis revealed a nanoporous surface architecture with mean values for the pore and ligament sizes similar to the ones determined from FE-SEM image analysis, thereby confirming the accuracy of the method. Average roughness of  $5.4 \pm 0.3$  nm was detected.

Additionally, the composition and thickness of the nanoporous oxide layer formed on the glassy alloy samples upon polarization at different potentials in the pseudo-passive region for 3600 s, were investigated by AES sputter depth profiling (Figure S4, Supporting Information). Only the main constituents Ti, Zr, and Cu as well as oxygen O of the  $\text{Ti}_{47}\text{Cu}_{38}\text{Zr}_{7.5}\text{Fe}_{2.5}\text{Sn}_2\text{Si}_1\text{Ag}_2$  alloy were considered, while the other minor constituents remained below a reliable detection



**Figure 8.** Oxide layer thickness values determined from AES chemical depth profiles of  $Ti_{47}Cu_{38}Zr_{7.5}Fe_{2.5}Sn_2Si_1Ag_2$  glassy ribbon samples (air side): air formed passive film on as-spun state and oxide layers obtained after potentiostatic polarization at different potentials in 5 M  $HNO_3$  at 60 °C for 3600 s; calculations are based on a standard sputter rate in  $SiO_2$  ( $6 \text{ nm min}^{-1}$ ).

limit for analysis. The profiles are very similar to the one presented in Section 3.2.2 after 3600 s at 1 V.

From the analysis of the oxygen depth profiles, the oxide layer thickness values were derived and they are exhibited in **Figure 8**. Compared to the low thickness <10 nm of the dense air-formed film on the as-spun ribbon surface, increasing the applied potential of the anodic treatment, generally increases the nanoporous layer thickness up to a value of about 34 nm at 1.4 V versus SCE.

In further studies, the possibility of increasing the oxide layer thickness with a longer anodization time at a passive potential was tested. As after 3600 s, the thickest nanoporous layer was obtained when applying 1.4 V versus SCE, this potential was selected to carry out the time-dependent investigation.

AES depth profiling analysis was performed on a glassy sample surface after 21 600 s (6 h) of the anodic treatment.

However, no increase of the layer was observed, on the contrary, there is a reduction of the oxide layer thickness from 34 nm after 3600 s (**Figure 9a**) to 24 nm after 6 h (**Figure 9b**). From the SEM image in **Figure 9c** in comparison to that in **Figure 5g**, it is revealed that prolonged anodization leads to less pronounced nanoporosity morphologies pointing to the formed nanoporous structures discussed in Section 3.2.2. Longer exposure times in concentrated  $HNO_3$  at anodic conditions may lead to the formation of hydrous oxides/ $TiO^{2+}$ , which are soluble in  $HNO_3$  and therefore decrease the thickness of the oxide film, as shown in the reaction mechanism in Section 3.2.2.

#### 4. Effect of the Surface Pretreatment on the Corrosion Behavior of the Glassy Ti Alloy in a Simulated Physiological Solution

The corrosion performance of glassy  $Ti_{47}Cu_{38}Zr_{7.5}Fe_{2.5}Sn_2Si_1Ag_2$  ribbon samples was analyzed in PBS solution at 37 °C and pH of 7.4 and, the impact of the pseudo-dealloying electrochemical pretreatment in 5 M  $HNO_3$  solution at 60 °C was evaluated. A pretreatment applying a potential of 1 V versus SCE for 3600 s was selected, as it yielded the best combination of a homogeneous nanoporous oxide layer with defined morphology and enhanced thickness, as well as a depleted Cu content in near-surface alloy regions, as described in the previous section.

Cp-Ti was used as a clinically relevant reference material and it was tested in polished and air-aged (nontreated) state and also, after the electrochemical pretreatment described above. This aimed at inducing passivation and rendering it more comparable to the surface states of the glassy ribbon samples. No relevant change in the cp-Ti surface after the pretreatment was observed (**Figure S5**, Supporting Information).

**Figure 10** shows exemplary linear potentiodynamic polarization curves of glassy alloy samples in air-aged as-spun state (nontreated) and after the pretreatment, as well as of cp-Ti samples nontreated and pretreated states. Mean values of current corrosion density ( $i_{corr}$ ), corrosion potential ( $E_{corr}$ ), and passive current density ( $i_{pass}$ ) at 1 V versus SCE are reported in **Table 2**.

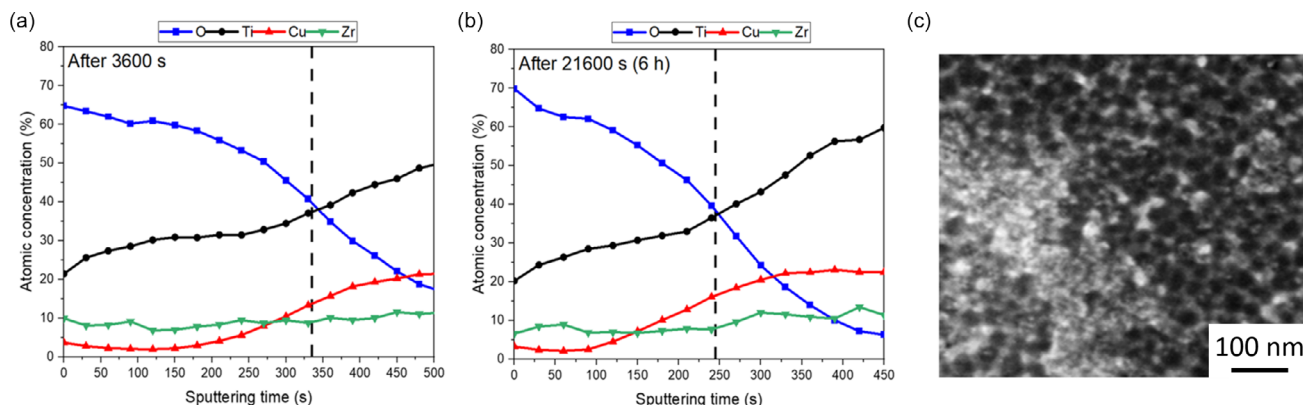


**Figure 9.** a) AES chemical depth profiles considering Ti, Zr, Cu, and O of the glassy  $Ti_{47}Cu_{38}Zr_{7.5}Fe_{2.5}Sn_2Si_1Ag_2$  alloy (air ribbon side) after polarization at 1.4 V versus SCE for 1 h and b) 6 h. Dashed vertical lines indicate the approximate extension of the oxide film, derived from the oxygen profile. c) FE-SEM image after potentiostatic polarization at 1.4 V versus SCE in 5 M  $HNO_3$  solution at 60 °C for 6 h.

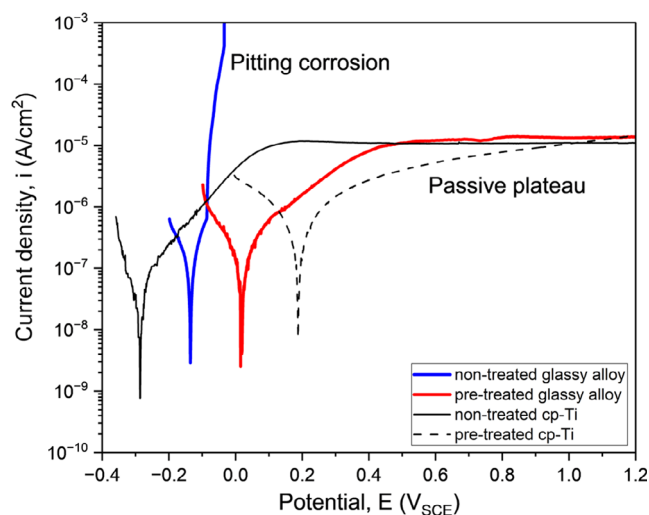


**Figure 10.** Potentiodynamic polarization curves measured in PBS (pH 7.4) at 37 °C for glassy  $\text{Ti}_{47}\text{Cu}_{38}\text{Zr}_{7.5}\text{Fe}_{2.5}\text{Sn}_2\text{Si}_1\text{Ag}_2$  ribbon samples and Ti sheets in air-aged or as-polished air-aged states (nontreated), respectively, and after anodic pretreatments at 1 V versus SCE for 3600 s in 5 M  $\text{HNO}_3$  solution at 60 °C.

**Table 2.** Corrosion parameters extrapolated from at least three different potentiodynamic polarization curves of  $\text{Ti}_{47}\text{Cu}_{38}\text{Zr}_{7.5}\text{Fe}_{2.5}\text{Sn}_2\text{Si}_1\text{Ag}_2$  and cp-Ti: corrosion current density ( $i_{\text{corr}}$ ), corrosion potential ( $E_{\text{corr}}$ ), and passive current density ( $i_{\text{pass}}$ ) measured at 1 V versus SCE.

Sample	$i_{\text{corr}}$ [ $10^{-8}$ A $\text{cm}^{-2}$ ]	$E_{\text{corr}}$ [V <sub>SCE</sub> ]	$i_{\text{pass}}$ [ $10^{-6}$ A $\text{cm}^{-2}$ ]
Nontreated cp-Ti	$5.5 \pm 2.5$	$-0.28 \pm 0.13$	$11.4 \pm 3.7$
Nontreated glassy alloy	$5.7 \pm 1.6$	$-0.13 \pm 0.01$	–
Pretreated glassy alloy	$5.5 \pm 2.5$	$0.03 \pm 0.05$	$12.0 \pm 1.5$
Pretreated cp-Ti	$17.8 \pm 20.1$	$0.19 \pm 0.01$	$13.3 \pm 3.5$

Under free corrosion conditions, (which are reflected by the low polarization regime near the initial current density minimum), a pretreatment effect is not yet evident.

In comparison to the nontreated cp-Ti, the nontreated glassy alloy shows more positive  $E_{\text{corr}}$  values, i.e., by about 150 mV. The potential effect is attributed to the multicomponent alloy composition with contribution from more noble constituents, e.g., Cu, (Fe, Sn, Ag). Already in the nontreated state, the glassy Ti–Cu-based alloy exhibits a very low corrosion density in the range of  $5.5\text{--}5.7 \times 10^{-8}$  A  $\text{cm}^{-2}$ . This is similar to the value for cp-Ti and hints to very low surface reactivities. For both materials, upon air-aging exposure and PBS pre-exposure at OCP for 60 min (not shown here), spontaneous passivation occurs. These very thin passive films of valve metal oxides, i.e., Ti-oxides, and for the alloy, Zr oxides, act as a strong barrier against free corrosive interaction with the chloride-containing solution. It has to be emphasized that, the experimental corrosion parameter values for the nontreated  $\text{Ti}_{47}\text{Cu}_{38}\text{Zr}_{7.5}\text{Fe}_{2.5}\text{Sn}_2\text{Si}_1\text{Ag}_2$  glassy alloy ribbon obtained here, agree reasonably well with literature data. Polished cross-sections of cast bulk samples of this glass-forming alloy were tested in PBS solution and similar low  $i_{\text{corr}}$  values in the range of  $5.5\text{--}5.7 \times 10^{-8}$  A  $\text{cm}^{-2}$  were determined.<sup>[14]</sup>

After the electrochemical pretreatment in 5 M  $\text{HNO}_3$ , for both materials, a significant positive shift of the  $E_{\text{corr}}$  value in the PBS solution is noticed in comparison to values measured for the nontreated states. The  $i_{\text{corr}}$  values remained at a very low level. This characteristic is explained by a transformation of the initially very thin oxide barriers from an air-aging process to the thicker Ti- and Zr-oxide layers generated by the pretreatment.

A reliable implant material must exhibit high corrosion resistance within the stability range of water, i.e., especially under anodic polarization conditions. Cp-Ti fulfills such a requirement even in a polished and air-aged (nontreated) state. The anodic polarization curve in Figure 10 demonstrates for nontreated cp-Ti in PBS the commonly known behavior of a direct transfer from the initial free corrosion state into a stable anodic passivity, characterized by a wide plateau with low passive current density values in the range of about  $11 \times 10^{-6}$  A  $\text{cm}^{-2}$ . On the contrary, the nontreated glassy Ti–Cu-based alloy does not fulfill the abovementioned requirement. Upon anodic polarization in PBS solution, it shows typical features of chloride-induced passivity breakdown and pitting corrosion. In Figure 10, this is characterized by the steep rise of the current density starting at about  $-0.09$  V versus SCE. An SEM image of such a ribbon surface after this polarization test in PBS is shown in Figure 11. A collection of pits (Figure 11a) and in higher resolution, a typical pit morphology (Figure 11b) can be observed on the air side of the ribbons. As mentioned in the introduction, the fundamental pitting corrosion mechanisms for these glass-forming alloys with the critical role of Cu-species being enriched in near-surface regions of only spontaneously passivated samples are known.<sup>[3,5,8,26–28]</sup> In the present study, the early passivity breakdown of the nontreated glassy  $\text{Ti}_{47}\text{Cu}_{38}\text{Zr}_{7.5}\text{Fe}_{2.5}\text{Sn}_2\text{Si}_1\text{Ag}_2$  alloy sample compared to reported literature data for bulk samples<sup>[14]</sup> must be attributed to the complex geometrical shape of the ribbons employed here.

The effect of an electrochemical pretreatment of the glassy alloy ribbons in a hot 5 M  $\text{HNO}_3$  solution toward suppression of the chloride-induced local corrosion processes is impressively demonstrated here. In Figure 10, the anodic polarization curve of a pretreated ribbon sample shows in the entire measured anodic potential regime a stable passive plateau with  $i_{\text{pass}}$  values of about  $12 \times 10^{-6}$  A  $\text{cm}^{-2}$  and no indications for passivity breakdown.

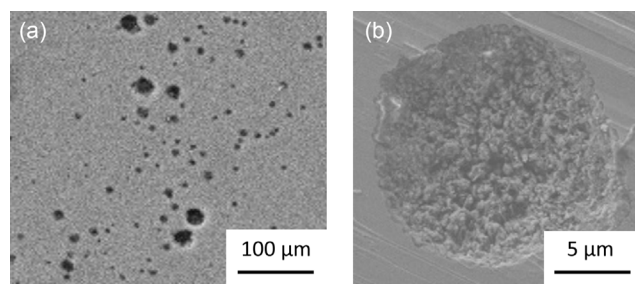


**Figure 11.** SEM images showing typical pit morphologies on surfaces of an air-aged as-spun (nontreated) glassy  $\text{Ti}_{47}\text{Cu}_{38}\text{Zr}_{7.5}\text{Fe}_{2.5}\text{Sn}_2\text{Si}_1\text{Ag}_2$  sample after potentiodynamic polarization in PBS (after interruption at a current density limit of  $1 \times 10^{-3}$  A  $\text{cm}^{-2}$ ), a) overview image and b) morphology of an individual pit.

This is similar to the behavior of the cp-Ti reference sample. Further, SEM examinations of the glassy samples after the test in PBS did not reveal the formation of corrosion pits (Figure S6, Supporting Information).

Obviously, the preformed surface states with thicker nanoporous Ti- and Zr-oxide layers and depleted Cu concentrations in near-surface regions of the glassy Ti–Cu-based alloy are stable in PBS solution and, they act as very effective barriers against chloride ion attack. Upon anodic polarization (i.e., positive charging) of a metal surface, the adsorption of negatively charged chloride ions is usually eased. In case of a nontreated glassy Ti–Cu-based alloy surface, the enrichment of noble Cu species directly underneath the spontaneously forming passive film of Ti (and Zr) oxides can enhance the chloride ion adsorption and therefore, support a breakdown of the very thin and defective passive film. This finally leads to pitting.<sup>[3,17,27,28]</sup> The depletion of the Cu concentration from near-surface regions of the glassy alloy together with the thicker oxide layers, obtained by the HNO<sub>3</sub> pretreatment, may have already weakened substantially the chloride ion adsorption processes and thus, suppressed the very initial step for pitting.

## 5. Summary and Conclusion

With the example of the bulk glass-forming Ti<sub>47</sub>Cu<sub>38</sub>Fe<sub>2.5</sub>Zr<sub>7.5</sub>Sn<sub>2</sub>Si<sub>1</sub>Ag<sub>2</sub> alloy, an electrochemical surface treatment approach for improving pitting corrosion resistance is presented. This treatment comprises potentiostatic polarization in the pseudo-passive potential regime of the glassy alloy in 5 M HNO<sub>3</sub> solution at 60 °C. It was demonstrated that these conditions are indispensable for inducing the desired surface transformation processes, defined as pseudo-dealloying. These lead to Cu-depletion in near-surface alloy regions and the generation of nanostructured valve metal oxide layers.

A mechanistic description of a possible pseudo-dealloying process was suggested: starting with an initial passive film formation, then a passivity breakdown with temporary Cu dissolution from near-surface regions, and eventually further, the gradual growth of the nanoporous oxide layers with a mixed composition of hydrous and nonhydrous Ti and Zr oxides. However, these surface processes on the glassy Ti–Cu-based alloy with no excess concentration of Cu (relative to valve metal components) are self-restrictive and therefore, the progression of the surface transformation front remains limited.

As a general trend, it can be concluded that, although at all pseudo-passive potentials such a process occurred, the most complete electrochemical pseudo-dealloying of the glassy Ti<sub>47</sub>Cu<sub>38</sub>Fe<sub>2.5</sub>Zr<sub>7.5</sub>Sn<sub>2</sub>Si<sub>1</sub>Ag<sub>2</sub> alloy surface was achieved by applying an anodic potential of 1 V versus SCE. This led to the most homogenous and defined nanoporous structure with the largest pores and finest ligaments. Increasing the potential led to the formation of wider ligaments and smaller pores in addition to a thicker oxide layer. Prolonged polarization up to 6 h did not substantially increase the layer thickness. Moreover, the nanoporous structure formation process is restricted to the pseudo-passive regime, since in transpassive conditions surface dissolution and degradation dominate.

Further, it was demonstrated that, such a pseudo-dealloying treatment is very effective for suppressing chloride-induced pitting corrosion of the glassy alloy in a simulated physiological solution. Within the anodic stability range of water, a stable passive behavior which is similar to that of cp-Ti, was obtained.

Thus, a strategy is proposed to overcome an obstacle for this type of bulk-glass-forming Ti–Cu-based alloy regarding possible application as implant material.

High GFA requires distinct alloy compositions, typically with high Cu contents. The resulting amorphous nature of the quenched alloy determines its beneficial mechanical performance. Our proposed surface treatment reduces the Cu content from near surface regions and enhances the corrosion resistance. Additionally, with view of other studies, e.g., nanoporous surfaces<sup>[33]</sup> or nanotubular oxide structures on Ti and Ti–Nb surfaces,<sup>[43]</sup> these generated surface states of the glassy alloy with nanoporous morphology of the oxide layers can provide promising nanotopographies that can stimulate the response of bone-forming cells. To analyze this is the subject of ongoing studies.

## Supporting Information

Supporting Information is available from the Wiley Online Library or from the author.

## Acknowledgements

The authors are grateful to K. Hennig, S. Donath, and A. Pöhl for sample preparation and technical support; B. Bartusch (DSC analysis), A. Voß (chemical analysis), S. Kaschube (AES analysis), and A. Koitzsch (XPS analysis). N.F.N. and A.G. are grateful for the financial support received from Deutsche Forschungsgemeinschaft (DFG) under the grant agreement no. 458057521; GE 1106/15-1. K.T., P.R. and A.G. acknowledge for funding the European commission within the H2020-MSCA grant agreement no. 861046 (BIOREMIA-ITN). V.S. and A.G. recognize Mercator Fellowship DFG project GE/1106/15-1 (no. 58057521). [Correction added on 03 May 2024, after first online publication: funding information has been added.]

Open Access funding enabled and organized by Projekt DEAL.

## Conflict of Interest

The authors declare no conflict of interest.

## Author Contributions

N.F.N.: writing -review and editing, writing-original draft, visualization, validation, methodology, investigation, formal analysis, data curation, and conceptualization. C.J.Q.: AFM measurements and analysis, spectroscopic analysis, scientific design and discussion, interpretation, writing, editing, and conceptualization. K.T.: scientific discussion, reviewing, and editing. M.H.: AES, XPS, and reviewing and editing. V.S.: scientific discussion, writing, editing, and conceptualization. N.P.: TEM, reviewing and editing. P.R.: reviewing, editing. M.Z.: reviewing, editing. A.G.: conceptualization, scientific discussion, writing, and editing.

## Data Availability Statement

The data that support the findings of this study are available from the corresponding author upon reasonable request.

## Keywords

dealloying, metallic glasses, pitting corrosion, surface treatments, Ti alloy

Received: December 21, 2023

Revised: April 4, 2024

Published online:

- [1] M. M. Trexler, N. N. Thadhani, *Prog. Mater. Sci.* **2010**, *55*, 759.
- [2] A. Inoue, A. Takeuchi, *Acta Mater.* **2011**, *59*, 2243.
- [3] J. R. Scully, A. Gebert, J. H. Payer, *J. Mater. Res.* **2007**, *22*, 302.
- [4] Y. Kirmanidou, M. Sidira, M. E. Drosou, V. Bennani, A. Bakopoulou, A. Tsouknidas, N. Michailidis, K. Michalakis, *Biomed Res. Int.* **2016**, *2016*, 2908570.
- [5] M. Bialy, M. Hasiak, A. Łaszcz, *J. Funct. Biomater.* **2022**, *13*, 245.
- [6] A. Sharma, V. Zadorozhnyy, *Metals* **2021**, *11*, 1933.
- [7] H. F. Li, Y. F. Zheng, *Acta Biomater.* **2016**, *36*, 1.
- [8] M. Calin, A. Gebert, A. C. Ghinea, P. F. Gostin, S. Abdi, C. Mickel, J. Eckert, *Mater. Sci. Eng., C* **2013**, *33*, 875.
- [9] A. Bandyopadhyay, I. Mitra, S. B. Goodman, M. Kumar, S. Bose, *Prog. Mater. Sci.* **2023**, *133*, 101053.
- [10] P. Du, B. Li, J. Chen, K. Li, G. Xie, *J. Alloys Compd.* **2005**, *404–406*, 657.
- [11] S. Bera, P. Ramasamy, D. Şopu, B. Sarac, J. Zálešák, C. Gammer, M. Stoica, M. Calin, J. Eckert, *J. Alloys Compd.* **2019**, *793*, 552.
- [12] C. H. Huang, Y. S. Huang, Y. S. Lin, C. H. Lin, J. C. Huang, C. H. Chen, J. B. Li, Y. H. Chen, J. S. C. Jang, *Mater. Sci. Eng., C* **2014**, *43*, 343.
- [13] Y. Liu, S. Pang, H. Li, Q. Hu, B. Chen, T. Zhang, *Intermetallics* **2016**, *72*, 36.
- [14] S. Pang, Y. Liu, H. Li, L. Sun, Y. Li, T. Zhang, *J. Alloys Compd.* **2015**, *625*, 323.
- [15] L. Deng, S. Wang, P. Wang, U. Kühn, S. Pauly, *Mater. Lett.* **2018**, *212*, 346.
- [16] P. Zhang, J. Tan, Y. Tian, H. Yan, Z. Yu, *Int. J. Adv. Manuf. Technol.* **2022**, *118*, 2017.
- [17] L. Deng, A. Gebert, L. Zhang, H. Y. Chen, D. D. Gu, U. Kühn, M. Zimmermann, K. Kosiba, S. Pauly, *Mater. Des.* **2020**, *189*, 108532.
- [18] C. Wang, N. Hua, Z. Liao, W. Yang, S. Pang, P. K. Liaw, T. Zhang, *Metall. Mater. Trans. A* **2021**, *52*, 1559.
- [19] J. J. Oak, G. W. Hwang, Y. H. Park, H. Kimura, S. Y. Yoon, A. Inoue, *J. Biomech. Sci. Eng.* **2009**, *4*, 384.
- [20] A. Liens, A. Etienne, P. Rivory, S. Balvay, J. M. Pelletier, S. Cardinal, D. Fabrègue, H. Kato, P. Steyer, T. Munhoz, J. Adrien, N. Courtois, D. J. Hartmann, J. Chevalier, *Materials* **2018**, *11*, 249.
- [21] Y. B. Wang, H. F. Li, Y. Cheng, Y. F. Zheng, L. Q. Ruan, *Mater. Sci. Eng., C* **2013**, *33*, 3489.
- [22] G. Xie, H. Kanetaka, H. Kato, F. Qin, W. Wang, *Intermetallics* **2019**, *105*, 153.
- [23] T. H. Li, P. C. Wong, S. F. Chang, P. H. Tsai, J. S. C. Jang, J. C. Huang, *Mater. Sci. Eng., C* **2017**, *75*, 1.
- [24] K. Jomova, M. Valko, *Toxicology* **2011**, *283*, 65.
- [25] E. V. Skorb, D. V. Andreeva, *Adv. Funct. Mater.* **2013**, *23*, 4483.
- [26] J. Fornell, E. Pellicer, N. Van Steenberge, S. González, A. Gebert, S. Suriñach, M. D. Baró, J. Sort, *Mater. Sci. Eng., A* **2013**, *559*, 159.
- [27] P. F. Gostin, D. Eigel, D. Grell, J. Eckert, E. Kerscher, A. Gebert, *J. Mater. Res.* **2014**, *30*, 233.
- [28] P. F. Gostin, O. Addison, A. P. Morrell, Y. Zhang, A. J. M. C. Cook, A. Liens, M. Stoica, K. Ignatyev, S. R. Street, J. Wu, Y. L. Chiu, A. J. Davenport, *Adv. Healthcare Mater.* **2018**, *7*, 1800338.
- [29] S.-I. Yamaura, S. Zhu, K. Abe, G. Xie, *Open J. Met.* **2014**, *4*, 56.
- [30] F. Qin, S. Zhu, Z. Dan, A. Kawashima, G. Xie, *J. Alloys Compd.* **2014**, *615*, S123.
- [31] M. L. Morrison, R. A. Buchanan, P. K. Liaw, B. A. Green, G. Y. Wang, C. T. Liu, J. A. Horton, *Mater. Sci. Eng., A* **2007**, *467*, 198.
- [32] D. Geissler, M. Uhlemann, A. Gebert, *Corros. Sci.* **2019**, *159*, 108057.
- [33] P. F. Gostin, A. Helth, A. Voss, R. Sueptitz, M. Calin, J. Eckert, A. Gebert, *J. Biomed. Mater. Res., Part B* **2013**, *101*, 269.
- [34] S. Abdi, S. Oswald, P. F. Gostin, A. Helth, J. Sort, M. D. Baró, M. Calin, L. Schultz, J. Eckert, A. Gebert, *J. Biomed. Mater. Res., Part B* **2016**, *104*, 27.
- [35] A. Lachová, M. Stoica, Š. Michalík, P. F. Gostin, M. Fujioka-Kobayashi, B. Schaller, J. F. Löffler, P. Sovák, *J. Alloys Compd.* **2023**, *940*, 168776.
- [36] R. Liu, K. Memarzadeh, B. Chang, Y. Zhang, Z. Ma, R. P. Allaker, L. Ren, K. Yang, *Sci. Rep.* **2016**, *6*, 29985.
- [37] P. Mandracci, F. Mussano, P. Rivolo, S. Carossa, *Coatings* **2016**, *6*, 7.
- [38] A. Revathi, A. D. Borrás, A. I. Muñoz, C. Richard, G. Manivasagam, *Mater. Sci. Eng., C* **2017**, *76*, 1354.
- [39] C. J. Querebillo, *Nanomaterials* **2023**, *13*, 982.
- [40] F. X. Qin, G. Q. Xie, X. M. Wang, T. Wada, M. Song, K. Furuya, M. Yoshimura, M. Tsukamoto, A. Inoue, *Mater. Trans.* **2009**, *50*, 1313.
- [41] F. X. Qin, X. M. Wang, T. Wada, G. Q. Xie, K. Asami, A. Inoue, *Mater. Trans.* **2009**, *50*, 605.
- [42] H. Sopha, D. Pohl, C. Damm, L. Hromadko, B. Rellinghaus, A. Gebert, J. M. Macak, *Mater. Sci. Eng., C* **2017**, *70*, 258.
- [43] A. Gebert, D. Eigel, P. F. Gostin, V. Hoffmann, M. Uhlemann, A. Helth, S. Pilz, R. Schmidt, M. Calin, M. Göttlicher, M. Rohne, J. Janek, *Surf. Coat. Technol.* **2016**, *302*, 88.
- [44] S. Abdi, M. Bönisch, S. Oswald, M. S. Khoshkhoo, W. Gruner, M. Lorenzetti, U. Wolff, M. Calin, J. Eckert, A. Gebert, *J. Mater. Res.* **2016**, *31*, 1264.
- [45] U. Wolff, A. Gebert, J. Eckert, L. Schultz, *J. Alloys Compd.* **2002**, *346*, 222.
- [46] C. Wang, M. Li, M. Zhu, H. Wang, C. Qin, W. Zhao, Z. Wang, *Nanomaterials* **2017**, *7*, 352.
- [47] F. Variola, J. H. Yi, L. Richert, J. D. Wuest, F. Rosei, A. Nanci, *Biomaterials* **2008**, *29*, 1285.
- [48] I. McCue, E. Benn, B. Gaskey, J. Erlebacher, *Annu. Rev. Mater. Res.* **2016**, *46*, 263.
- [49] J. Weissmüller, K. Sieradzki, *MRS Bull.* **2018**, *43*, 14.
- [50] E. M. Paschalidou, F. Scaglione, A. Gebert, S. Oswald, P. Rizzi, L. Battezzati, *J. Alloys Compd.* **2016**, *667*, 302.
- [51] L. Mihaylov, A. Inoue, L. Lyubenova, D. Nihtianova, T. Spassov, *Intermetallics* **2018**, *98*, 148.
- [52] M. Pourbaix, H. Zhang, A. Pourbaix, *Presentation of an Atlas of Chemical and Electrochemical Equilibria in the Presence of a Gaseous Phase*, National Association of Corrosion Engineers **1974**.
- [53] A. Blanquer, A. Hynowska, C. Nogués, E. Ibáñez, J. Sort, M. D. Baró, B. Özkale, S. Pané, E. Pellicer, L. Barrios, *PLoS One* **2016**, *11*, e0156644.
- [54] S. L. Zhu, J. L. He, X. J. Yang, Z. D. Cui, L. L. Pi, *Electrochem. Commun.* **2011**, *13*, 250.
- [55] S. Zhu, G. Xie, X. Yang, Z. Cui, *Mater. Res. Bull.* **2013**, *48*, 1961.
- [56] A. Gebert, P. F. Gostin, L. Schultz, *Corros. Sci.* **2010**, *52*, 1711.
- [57] U. K. Mudali, S. Baunack, J. Eckert, L. Schultz, A. Gebert, *J. Alloys Compd.* **2004**, *377*, 290.
- [58] S. Oswald, P. F. Gostin, A. Helth, S. Abdi, L. Giebeler, H. Wendrock, M. Calin, J. Eckert, A. Gebert, *Surf. Interface Anal.* **2014**, *46*, 683.
- [59] M. C. Biesinger, L. W. M. Lau, A. R. Gerson, R. S. C. Smart, *Appl. Surf. Sci.* **2010**, *257*, 887.
- [60] M. C. Biesinger, *Surf. Interface Anal.* **2017**, *49*, 1325.